PAPER • **OPEN ACCESS**

Triangular quantum photonic devices with integrated detectors in silicon carbide

To cite this article: Sridhar Majety *et al* 2023 *Mater. Quantum. Technol.* **3** 015004

Materials for Quantum Technology

PAPER

Triangular quantum photonic devices with integrated detectors in silicon carbide

Sridhar Majety[1,*], Stefan Strohauer[2], Pranta Saha[1], Fabian Wietschorke[3], Jonathan J Finley[2], Kai Müller[3] and Marina Radulaski[1]

[1] Department of Electrical and Computer Engineering, University of California, Davis, CA 95616, United States of America
[2] Walter Schottky Institut, School of Natural Sciences, and MCQST, Technische Universität München,Am Coulombwall 4, 85748 Garching, Germany
[3] Walter Schottky Institut, School of Computation, Information and Technology, and MCQST, Technische Universität München, Am Coulombwall 4, 85748 Garching, Germany
* Author to whom any correspondence should be addressed.

E-mail: smajety@ucdavis.edu

Keywords: silicon carbide, photonic crystals, waveguides, superconducting single photon detectors, quantum information processing, color centers, triangular cross-section photonics

OPEN ACCESS

RECEIVED
11 August 2022

REVISED
22 February 2023

ACCEPTED FOR PUBLICATION
9 March 2023

PUBLISHED
22 March 2023

Abstract

Triangular cross-section silicon carbide (SiC) photonic devices have been studied as an efficient and scalable route for integration of color centers into quantum hardware. In this work, we explore efficient collection and detection of color center emission in a triangular cross-section SiC waveguide by introducing a photonic crystal mirror on its one side and a superconducting nanowire single photon detector (SNSPD) on the other. Our modeled triangular cross-section devices with a randomly positioned emitter have a maximum coupling efficiency of 89% into the desired optical mode and a high coupling efficiency (>75%) in more than half of the configurations. For the first time, NbTiN thin films were sputtered on 4H-SiC and the electrical and optical properties of the thin films were measured. We found that the transport properties are similar to the case of NbTiN on SiO_2 substrates, while the extinction coefficient is up to 50% higher for 1680 nm wavelength. Finally, we performed finite-difference time-domain simulations of triangular cross-section waveguide integrated with an SNSPD to identify optimal nanowire geometries for efficient detection of light from transverse electric and transverse magnetic polarized modes.

1. Introduction

Color centers in silicon carbide (SiC) have been a prominently studied quantum platform for applications in quantum information processing (QIP). Their unique combination of spectral homogeneity, emission at near infra-red and telecommunication wavelengths, long spin coherence, and spin-photon entangling processes offer key applications in quantum communication, simulation, computing, and sensing [1–7].

The optical response of a color center has a sharp peak called the zero phonon line (ZPL) and a broad phonon side band (PSB). Emission through ZPL, when there is no dephasing, results in indistinguishable photon creation necessary for QIP applications. Integration of color centers with photonic devices is an important step toward their performance improvement and scalability, as shown in explorations with SiC pillars [8, 9], waveguides [10, 11], and micro- and nano-resonators [11–15]. Moreover, recent results on growth and patterning of superconducting NbN on 3 C-SiC [16, 17] for use as the superconducting nanowire single photon detectors (SNSPDs) indicates that quantum circuitry can be further miniaturized and optimized.

The challenges in maintaining the pristine quality of color centers have led photonic integration away from the established nanofabrication processes and toward alternative approaches that require non-standard sample preparation [11, 13, 18] or angled etching [10, 19, 20]. The latter, in particular, has been explored for its potential in wafer-scale processing [21]. Angle etching produces triangularly shaped devices whose

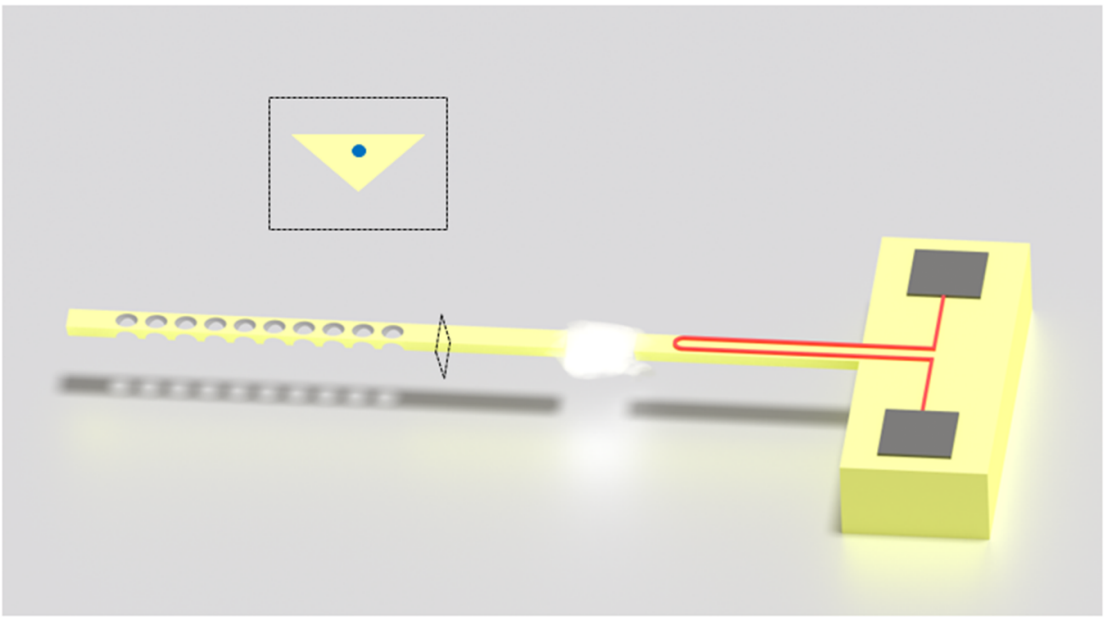

Figure 1. Illustration of SNSPD integrated onto a photonic device with a color center. Single color center is positioned in the waveguide region such that the dipole emission reflected by the photonic crystal mirror constructively interferes with the dipole emission into the waveguide region. The cloud region in the waveguide represents the segment where the pump light is filtered (e.g. by a ring oscillator or an inversely designed structure) to prevent any SNSPD saturation. Single photon detection is performed by the SNSPDs through absorption of the dipole emission in the waveguide. (Inset) The cross-section view of the structure, showing the color center (blue) optimally positioned at the centroid of the triangular waveguide profile.

photonic modes have been recently studied in terms of waveguide propagation [10, 22], photonic crystal (PC) band gap formation [23], PC cavity resonances [22], and grating coupler performance [24].

In this paper, we expand on the studies of triangular SiC photonics by focusing on methods to optimize collection and detection of color center light by integration with a PC mirror (PCM) and an SNSPD, as illustrated in figure 1. In particular, we study the case of the nitrogen vacancy (NV) in 4H-SiC with emission wavelengths in the range 1176 nm–1243 nm [25–27]. When placed in a symmetric waveguide, at least half of the light is lost in an undesired direction, but this can be circumvented by the addition of a PCM. PCM has a periodic variation of refractive index, which results in the formation of photonic band gaps. Understanding the formation of these band gaps is necessary for applications in selective reflection of the ZPL and PSB emissions with the goal of enhancing light collection efficiency [23]. The other side of the waveguide deals with the efficient detection through hybrid integration with NbTiN SNSPDs. The SNSPDs are the leading detectors in terms of quantum efficiency, low dark counts and low timing jitter. Moreover, they offer an on-chip detection that overcomes the losses involved in the off-chip detection, thus boosting the success rate of QIP protocols [28]. However, depending on the type of excitation, the pump laser used for an off-resonant excitation of the color center can scatter into the detector region and saturate the SNSPD. There have been successful demonstrations to suppress the stray pump laser by coating the backside of the chip with an absorbing material [29] and masking the inactive regions of the chip [30]. To further suppress the pump laser coupled into the waveguide, spectral filters like ring resonators [31, 32] and inverse-designed structures [33, 34] can be integrated in the waveguide region before the detectors, with implementation in the illustrated cloud segment in figure 1.

We first find the 1D PC conditions for band gap formation in triangular geometry on the desired wavelength domain (NV in 4H-SiC in this work) using the plane wave expansion (PWE) and the finite-difference time-domain (FDTD) methods. We then utilize the optimal PC design as a PCM in a triangular waveguide and study the role of color center positioning in obtaining high emission coupling to the propagating optical mode. Finally, in a combination of experimental and modeling approaches, we study the triangular waveguide mode absorption by a NbTiN SNSPD.

2. PCs for efficient propagation of color center emission in a triangular waveguide

Color centers have an optical dipole-like emission covering a solid angle of 4π [10]. This causes 50% higher than in spin-entangled photon loss in the triangular cross-section waveguide resulting in low collection efficiency. An *in situ* mirror, capable of reflecting color center emission, should theoretically double the

collection efficiency. It is possible to design such a structure artificially by periodic variation of the dielectric contrast, known as the PC [35]. For enhanced collection, we deliberately open up a gap possessing the NV center emission wavelength in the photonic bands, which is achievable by making a particular choice of PC parameters [36].

Waveguides support light propagation in a particular direction via total internal reflection. We implement 1D PC in our triangular cross-section waveguide to introduce asymmetry for redirecting the color center emission. However, 1D PCMs have mostly been realized in conventional rectangular geometry [37–39], and photonics with triangular geometry has been focused on making efficient active photonic devices [7, 22, 40]. Photonic band structures in triangular geometry have not been studied in detail. In this light, our recent work provides an insightful explanation of the dispersion relations in SiC triangular geometry [23]. From the band structures obtained from PWE method, we use FDTD method to analyze the performance of the triangular-cross section 1D PCM and the dependence of the coupling efficiency to the waveguide mode on the emitter position with respect to the PCM.

2.1. Considerations for integrating color centers into triangular cross-section devices

Color centers in SiC have multiple orientations due to the presence of inequivalent lattice sites (h, k). The dipole orientations of the color centers can be parallel (silicon vacancy in SiC) or at an angle (NV center in SiC) to the crystal axis (*c*-axis). In a photonic device fabricated from commonly available 4H-SiC, grown along the *c*-plane, this would result in emissions strongly coupling to the fundamental TM (f-TM) mode [8]. On the other hand, it has been shown that using 4H-SiC grown along the *a*-plane, the color center emission can be predominantly coupled to the fundamental TE (f-TE) mode [10].

Triangular cross-section waveguides support f-TE/TM modes and other higher order modes [22]. The fraction of a color center emission coupling to a supported waveguide mode depends on the position of the emitter within the triangular cross-section. Highest coupling to a mode can be achieved by positioning the emitter at the maximum intensity point of that mode. The maximum intensity point of the f-TE mode is located approximately at the centroid of the triangle, which is an optimal color center position for achieving highest coupling efficiency to the f-TE mode [10, 22].

The depth of the centroid from the surface depends on the width and etch angle of the triangular cross-section waveguide. These dimensions can be decided on the basis of the implantation capabilities, to ensure that the implanted color centers achieve the highest coupling efficiency to the f-TE mode. For a given emission wavelength, a triangular cross-section waveguide has an optimal width at which it has single mode propagation (f-TE), with high (>80%) coupling to the f-TE mode [10]. Single mode propagation in the waveguide is key for applications in QIP [41, 42]. The optimal width of the triangular cross-section devices increases with the etch angle and emission wavelength. Hence, triangular cross-section devices with larger etch angles have more fabrication friendly dimensions. Moreover, they require shallow implantation depths, which causes less damage to the crystal and having an emitter closer to the surface is useful for SNSPD absorption. Advantages like single mode propagation with high coupling efficiency, less damage to the crystal and better detection in SNSPD outweighs the overall effect of the color center emission lost into the f-TM or other modes.

2.2. Waveguide design with TE and TM band gap

NV center emission in SiC has both TE- and TM-like components [43]. Therefore, a PCM with polarization-independence is necessary to increase collection efficiency. For broadband reflectivity, such a mirror must have as large a complete photonic band gap as possible [44, 45]. Single mode propagation [41, 42] and positioning of emitter at the centroid of the triangular cross-section [10, 22] ensures that most of the color center emission is coupled into the waveguide. It was shown that 45° etch angle has predicted the best results for the complete band gap [23]. But in this study, an etch angle of 60° was chosen because the optimal emitter position is closer to the top surface, offering realistic implantation depths (70 nm) and efficient absorption in the SNSPDs. Moreover, a 60° etch angle supports single mode propagation for larger dimensions than in the case of 45° [10], resulting in a more fabrication friendly waveguide design. The width of the waveguide was set to 800 nm, as it supports the f-TE and f-TM modes only.

The 1D PC is made of cylindrical air holes in a triangular cross-section SiC waveguide as shown in figure 2(a). The parameters are as follows: periodicity along the *y* axis *a*, waveguide width *w*, hole radius *r*, and etch angle α, which corresponds to half-angle at the apex. The refractive index of SiC is considered 2.6 for all the simulations. In this study, we focused on the dispersion relations for $\alpha = 60°$ w.r.t *w* and *r*. We vary *w* from 1.2*a* to 2.25*a* and *r* from 0.25*a* to 0.45*a*. The band structure in figure 2(b) exhibits three properties: (i) a wide TE band gap, (ii) a narrow TM band gap, and (iii) a partial overlap between TE and TM band gaps, which is the complete photonic band gap. Figure 2(c) delineates the changes in the TE/TM gap (c/a) and the corresponding gap size (gap-midgap ratio) with r/a for *w* values of 1.2a, 1.35a and 1.5a. Midgap frequency

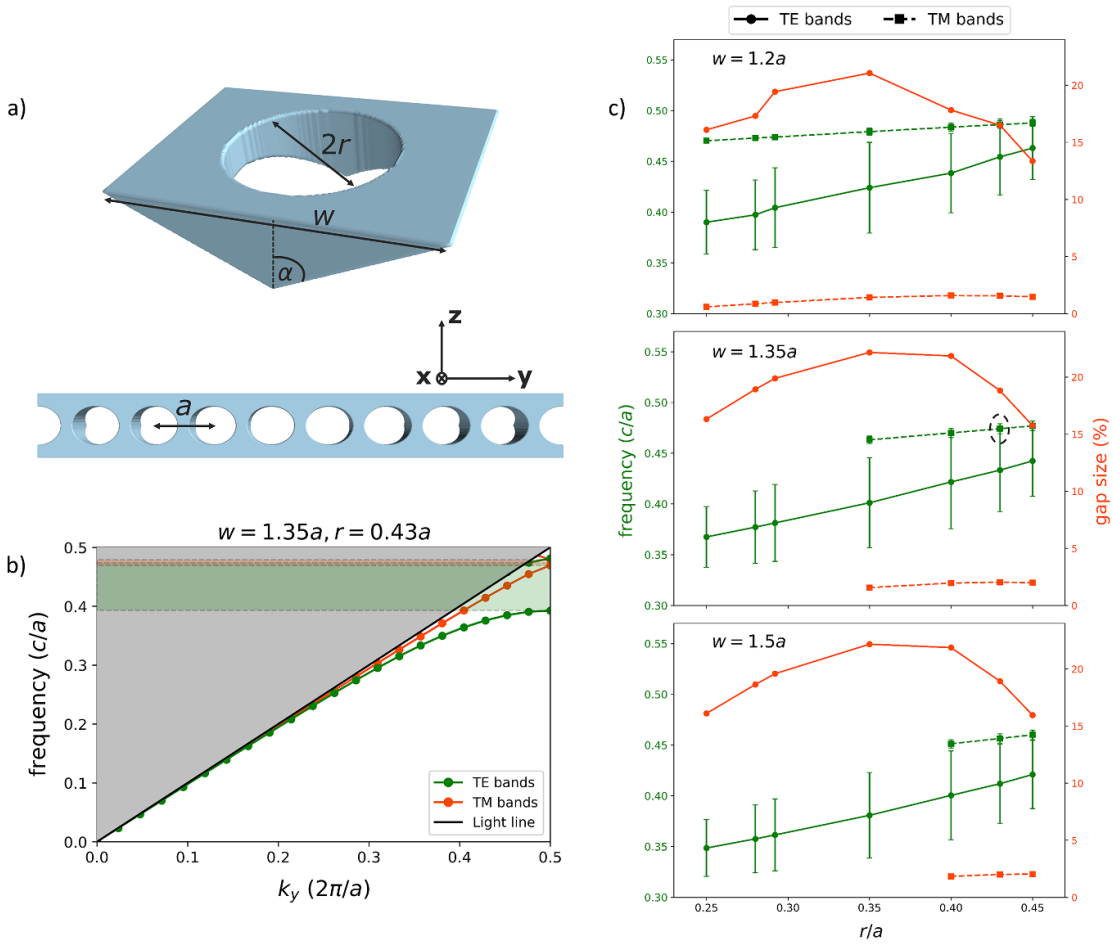

Figure 2. (a) Unit cell of the 1D PC structure. (b) Band structure for $\alpha = 60°$, $w = 1.35a$, and $r = 0.43a$. (c) TE/TM photonic band gap and gap size as a function of normalized hole radii for $w = 1.2a, 1.35a, 1.5a$ respectively. Center point indicates midgap frequency and error bar indicates gap width for the corresponding TE/TM modes. The dashed circle shows the TE-TM gap overlap for the band structure shown in (b).

increases with r/a for both TE and TM band gaps as volumetric fill factor (VFF) and effective refractive index (n_{eff}) have an inverse relationship with r/a [23]. Gap size initially increases with r/a as fewer propagating modes are supported, but declines after the maximum value is reached. Though this trend is observed for both TE and TM bands, the TM band gap completely vanishes for larger widths ($w > 1.5a$). Moreover, the highest TE gap size (∼22%) is an order magnitude higher compared to the highest TM gap size (∼2%), which is attributed to the connectivity between high-dielectric regions [35]. In general, complete band gap mostly occurs for smaller widths with larger hole radii as depicted in figure 2(c). Nevertheless, the choice of parameters for designing the reflector is made in such a way that there is a balance between optimal band gap size and reproducibility of the nanofabrication.

2.3. SiC waveguide design with a PCM

In this section, we use the PC parameters from the PWE method and simulate a triangular cross-section waveguide with a reflector, using the FDTD package in Lumerical [10, 22]. This allows for a comparison of the band gap position estimated from the two different methods, PWE and FDTD. The FDTD method uses the Fourier transform of the time-domain signal to record the field data in the frequency domain. To increase the collection efficiency of the photons from the ZPL and PSB of the NV center in SiC, the PC parameters were chosen to have a band gap spanning these emission wavelengths. As mentioned in section 2.2, the size of the TM band gap (and thus the complete band gap) is significantly smaller than the size of the TE band gap, limiting the reflected wavelengths of both TE- and TM-like components of the NV center emission.

In this study, we focus on two sets of parameters for the PC (1) complete band gap and (2) NV optimized band gap, for a waveguide with $w = 800$ nm and $\alpha = 60°$. In the first scenario, the complete band gap was achieved using PC parameters of $r = 237$ nm and $a = 593$ nm, with a complete band gap from 1268 nm to 1274 nm (TE band gap: 1268 nm to 1579 nm, TM band gap: 1249 nm to 1274 nm), which is outside the emission wavelength range of the NV center. In the second scenario, PC parameters of $r = 213$ nm and

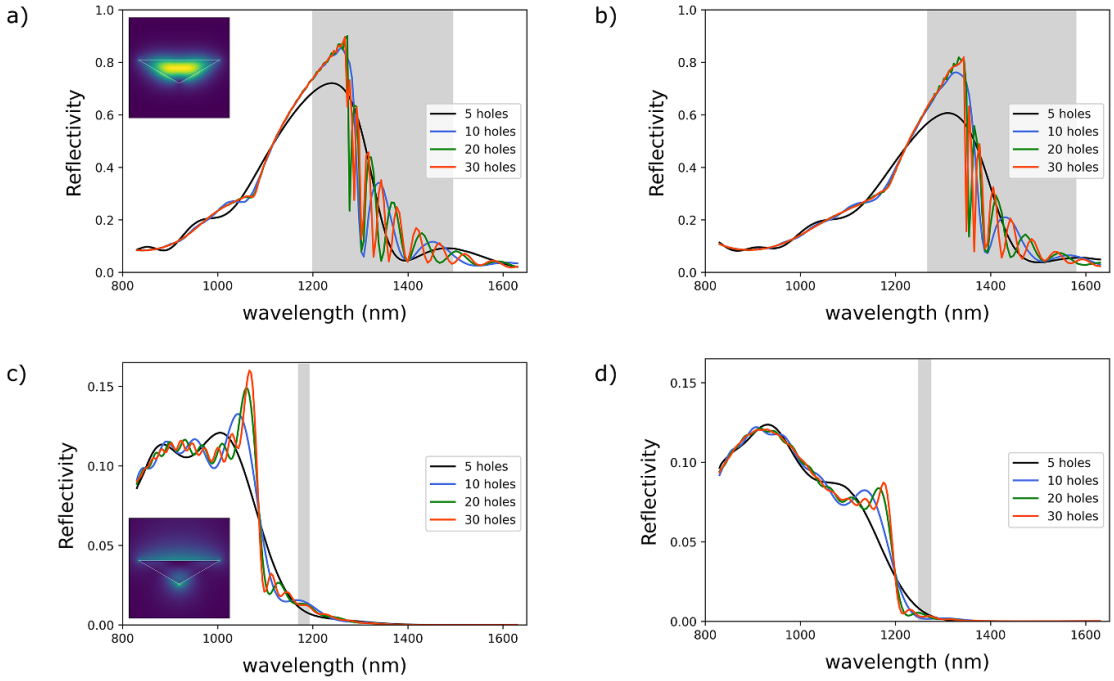

Figure 3. The reflectivity of PCM as a function of wavelength for varying number of air holes. Grey regions indicate the band gap values calculated from the PWE method. (a) Reflectivity of the f-TE mode for a NV optimized design. Inset shows the mode profile of the f-TE mode of the waveguide at 1230 nm. (b) Reflectivity of the f-TE mode for a complete band gap design. (c) Reflectivity of the f-TM mode for a NV optimized design. Inset shows the mode profile of the f-TM mode of the waveguide at 1230 nm. (d) Reflectivity of the f-TM mode for a complete band gap design.

$a = 533$ nm were chosen, resulting in both TE (1200 nm–1494 nm) and TM (1170 nm–1192 nm) band gaps individually overlapping with the emission wavelength range of NV centers, but no complete band gap.

As the number of air holes increases, the maximum reflectivity of the PCM increases and saturates for 20 air holes, as shown in figures 3(a) and (b). It is observed that the FDTD calculated wavelength for maximum reflectivity deviates from the center of the PWE calculated bandgap (grey region) [46]. The reflectivity curve has a full width half maximum of ∼200 nm, large enough to reflect the ZPL and the entire PSB of the color center emission. At 1230 nm, the NV optimized design has ∼85% reflectivity for the f-TE mode. The reflectivity at a given wavelength depends on two factors: (1) the effective index of the f-TE mode (n_{eff}) and (2) the fraction of color center emission coupled into the waveguide. While n_{eff} decreases monotonically with an increased wavelength, the coupling efficiency rises to the optimal point (designed at 1230 nm) and subsequently decreases. The combination of the two effects cause the reflectivity to gradually increase for the short wavelengths and sharply drop for the long wavelengths. In the case of the f-TM modes, the reflectivity values are relatively lower due to the low coupling efficiency to the f-TM mode (∼20%) and evanescent loss to the surroundings ($n_{\text{eff}} = 1.09$).

When a dipole emitter (1230 nm) is positioned at the centroid of the triangular cross-section (∼70 nm depth) of the waveguide ($w = 800$ nm, $\alpha = 60°$), 44% of the 50% light in each direction of the waveguide is coupled to the f-TE mode ($n_{\text{eff}} = 1.574$). In the presence of a PCM, the 50% dipole emission directed toward the PCM is reflected back towards the emitter, causing interference with the emission propagating in the waveguide region (indicated by a brown arrow in figure 4(a)). We observe that as the distance between the emitter and the PCM (s) is varied, the total light coupled to the f-TE mode varies periodically, as shown in figure 4(b). Constructive (destructive) interference occurs if the additional distance $2s$ traveled by the reflected wave results in a phase difference that is an even (odd) multiple of π. The periodicity of the coupling efficiency matches with the calculated value ($\lambda/n_{\text{eff}} = 390$ nm) and the maximum coupling efficiency of 89% is achieved for values of s that are integer multiples of ∼390 nm. There exists a 200 nm region with coupling efficiency >75%. Thus, any randomly positioned emitter in the waveguide has at least 50% chance of being at a position with high coupling efficiency.

3. Integrated SNSPDs for efficient detection of light in triangular waveguides

For single-photon detection, SNSPDs [47] provide unrivaled performance metrics such as high detection efficiency, including at 1550 nm wavelength [48], high count rate, low dark-count rate [49], and high

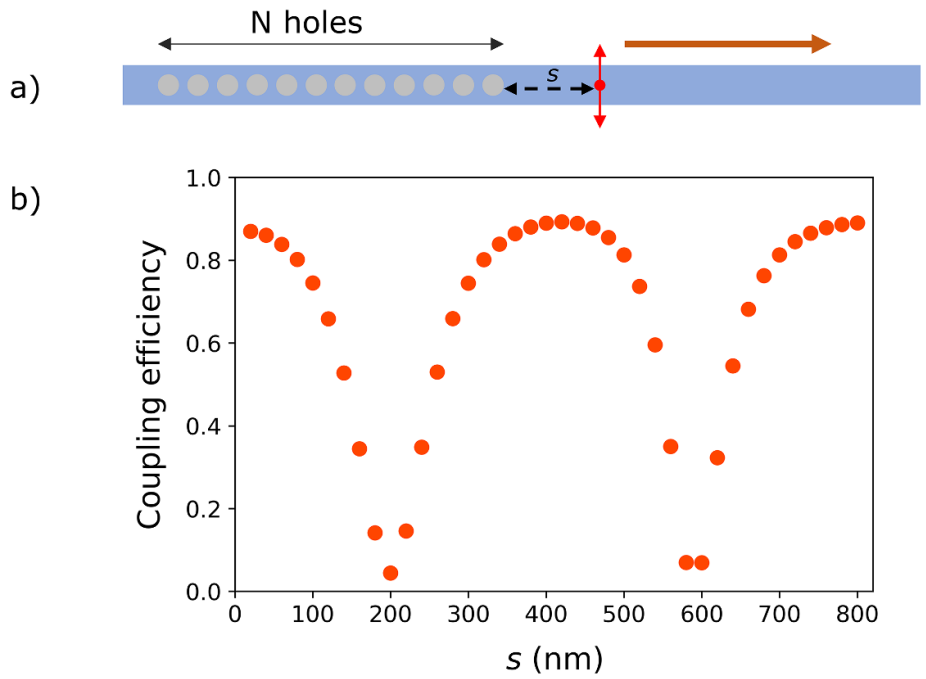

Figure 4. (a) Top view of the waveguide design with reflector having N air holes. The color center (red dot with red arrows indicating the dipole orientation) is positioned at a distance *s* from the edge of the first hole and its emission propagation indicated by the arrow (brown). (b) The variation of the coupling efficiency of the color center emission to the f-TE mode, in the direction of propagation, as a function of the color center's position (*s*) from the photonic crystal.

temporal resolution [50]. As such, they have found many applications in quantum communication and information processing as well as in high energy physics for charged particle detection [51–53]. Compared to the top-illumination of meander SNSPDs and the enhancement of their detection efficiency by use of an optical cavity with a mirror underneath [54, 55], short waveguide integrated SNSPDs avoid coupling losses when being interfaced with on-chip devices and provide smaller recovery times as a result of their lower kinetic inductance [56, 57]. Due to their superior performance metrics, in this section we study the potential of integrating SNSPDs onto triangular cross-section SiC waveguides to detect single-photon emission from color centers embedded in the waveguide. We start by investigating the fundamental properties of NbTiN films on SiC substrates and subsequently provide performance estimates for SNSPDs on SiC. Next, we use FDTD simulations to determine the coupling efficiency from triangular SiC waveguides to SNSPDs integrated on top of the waveguide and its dependence on the detector geometry.

3.1. Optical and transport properties of NbTiN thin films on SiC

In this section, we investigate the optical and the transport properties of NbTiN thin films on SiC substrates. For this, we used DC reactive magnetron sputtering at room temperature with an Ar/N_2 atmosphere and a sputtering target with the stoichiometry $Nb_{0.7}Ti_{0.3}$ to fabricate the NbTiN films studied in the following.

For simulation of absorption in NbTiN SNSPDs on triangular cross-section SiC waveguides, the optical constants of the deposited superconductor are essential, especially because the optical and the transport properties vary with deposition parameters and the underlying substrates [58]. We used a variable angle spectroscopic ellipsometer, Model M-2000 of J A Woollam Co., to measure the optical constants over a wavelength range of 210 nm to 1687 nm. As NbTiN is absorbing at all measurement wavelengths and one cannot resort to a transparent wavelength window, it is difficult to decouple and determine the optical constants and film thickness simultaneously due to correlations between both. However, this correlation can be overcome by measuring with the interference enhancement method, where the film is measured on an additional thick transparent dielectric layer and at multiple angles [59–61]. As we measured the NbTiN films on two-sided polished SiC substrates, two additional challenges emerge: The occurrence of reflections on the back side of the substrate, as well as the fact that SiC is a birefringent material. However, similar to the interference enhancement method, the anisotropy helps in decoupling thickness and optical constants for the NbTiN film [62]. Including backside reflections of the uniaxial 4H-SiC substrate in the model, we obtain a fitting of the measured data with a mean square error less than 5, indicating good agreement between the model and the measured data. The resulting optical constants, shown in figure 5, reveal a smaller extinction coefficient *k* and a higher refractive index *n* for the thicker film and provide the basis for the subsequent

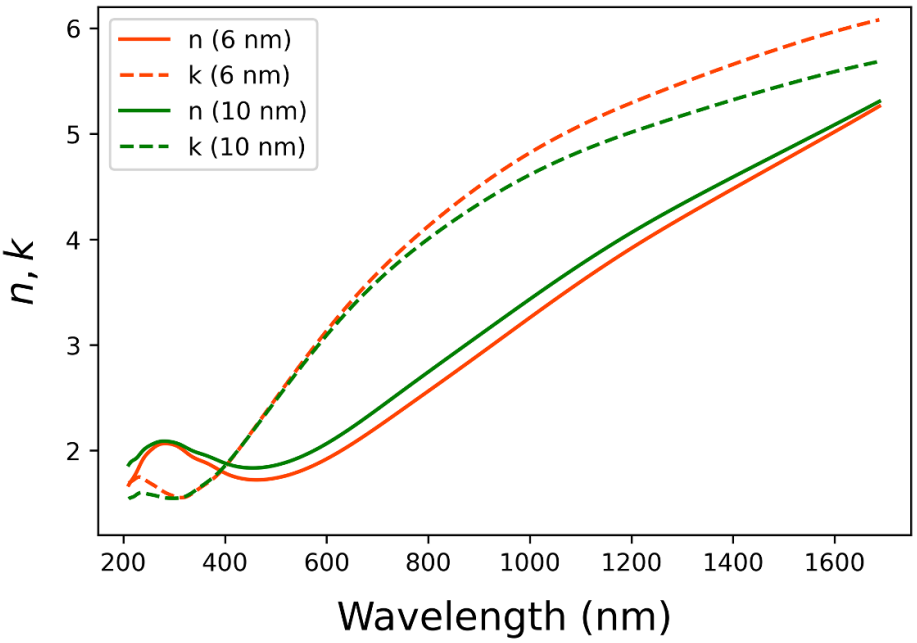

Figure 5. Extinction coefficient k and refractive index n of 6 nm and 10 nm NbTiN films on 4H-SiC substrates.

FDTD simulations. Compared to the optical constants of a 5.5 nm thick NbTiN film grown by sputtering on silicon substrates in the publication of Banerjee *et al* [59], we obtain similar results, although our data shows no features in the range from 500 nm to 1000 nm and our refractive index is ∼20% and the extinction coefficient ∼50% higher for a wavelength of 1680 nm. This agrees with the fact that the growth and properties of polycrystalline materials such as NbTiN depend on the underlying substrate.

As fabrication and characterization of SNSPDs is technologically challenging and time consuming, it is beneficial to estimate the detector performance directly from properties of the sputtered films—especially when it comes to new superconducting materials or different substrates. To assess, for example, possible operating temperatures of the envisioned SNSPDs, it is essential to know the device's critical temperature T_c at which it switches from the superconducting to the normal conducting state. As this temperature is reduced for nanowires compared to thin films or bulk material [63, 64], the critical temperature of the film provides an upper limit for reachable SNSPD critical temperatures. Furthermore, by measuring fundamental film transport properties such as sheet resistance R_{sheet}, quasiparticle diffusivity D [65, 66], and Hall coefficient R_H, we can estimate key detector metrics such as depairing current I_{dep} (an upper limit for the detector's switching current) and fall time τ_{fall}, and obtain information about disorder in the film (via the deduced Ioffe-Regel parameter $k_F l$ [67]). The depairing current density at a temperature T can be calculated according to the Bardeen model [65, 68–70] from the superconductor's energy gap $\Delta(0\text{K}) = 2.0\, k_B\, T_c$ with the factor 2.0 for NbTiN according to [71, 72], the elementary charge e, the resistivity in the normal conducting state ρ_{nc}, and the quasiparticle diffusivity D by:

$$j_{\text{dep}}(T) = 0.74 \cdot \frac{(\Delta(0\text{K}))^{3/2}}{e\rho_{\text{nc}}\sqrt{\hbar D}} \left(1 - \left(\frac{T}{T_c}\right)^2\right)^{3/2}. \tag{1}$$

A higher switching current of the detector also means a higher amplitude of the detection pulse, which is beneficial for the signal-to-noise ratio.

Moreover, we can calculate the kinetic inductance from the sheet resistance R_{sheet}, the energy gap Δ, and the nanowire width w and length l [65, 73]:

$$L_k = \frac{\hbar R_{\text{sheet}}}{\pi \Delta(0\text{K})} \frac{l}{w}, \tag{2}$$

that can be used to estimate the fall time of a detection pulse [74, 75] by

$$\tau_{\text{fall}} = \frac{L_k}{R_{\text{load}}}, \tag{3}$$

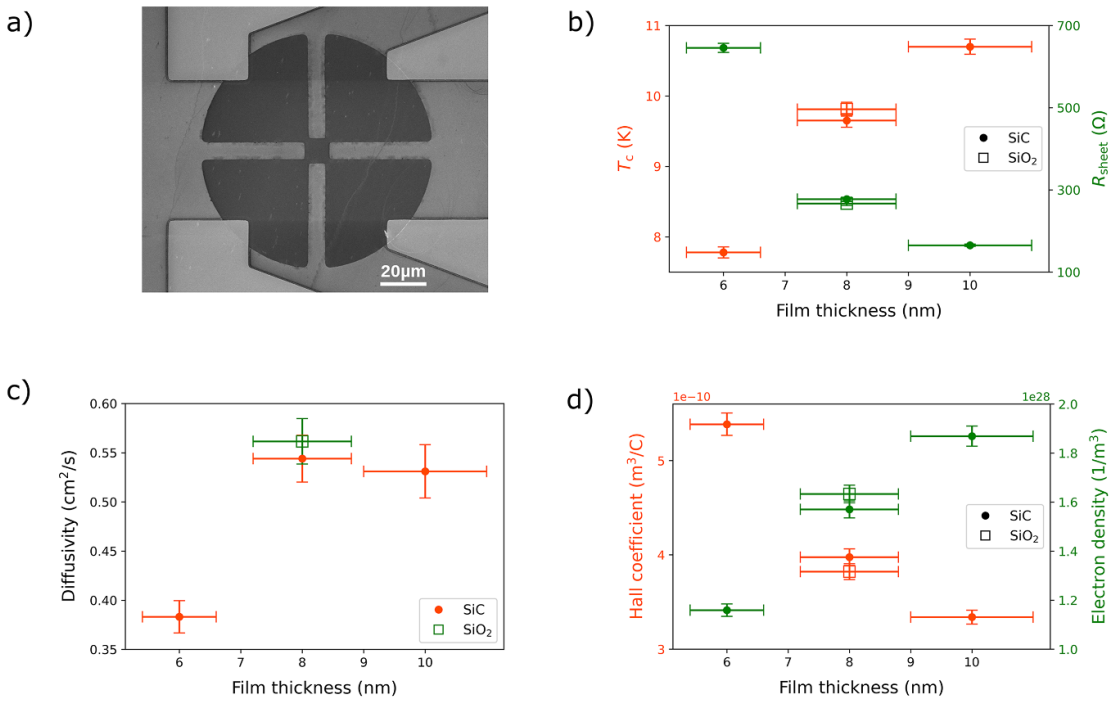

Figure 6. Critical temperature and transport measurements of sputtered NbTiN on 4H-SiC substrates. (a) shows an SEM image of the fabricated cloverleaf structures that were used for performing the magneto-transport measurements. In graphs (b)–(d), the measured data is shown for films of nominal thicknesses 6 nm, 8 nm, and 10 nm.

with R_{load} denoting the load resistor, which can be either a shunt resistor or the readout electronics (typically 50 Ω). From the fall time, we can also estimate the maximum count rate by $1/\tau_{fall}$. In figure 6, we show the measured transport properties of 6 nm, 8 nm, and 10 nm sputtered NbTiN[4] on 4H-SiC substrates with one 8 nm film of the same sputtering round on a silicon wafer with thermally grown SiO_2 as reference substrate. From this fundamental data, we calculate estimates for key detector metrics in table 1. Despite the difference in refractive index and extinction coefficient found above, a comparison of the measured and derived performance metrics for NbTiN SNSPDs on SiC substrates with reference to NbTiN SNSPDs on SiO_2 substrate yields similar values. Also, our measured transport data agree with the literature [67, 76, 77]. However, it seems worthwhile to note that our data for the electron density is lower than the values found in the literature. Nevertheless, when comparing the data in [67, 76], the electron density shows a dependence on the stoichiometry of $Nb_xTi_{1-x}N$, and our case with $x = 0.7$ fits into the picture of having a minimum between $x = 0.66$ and $x = 0.86$.

We conclude that choosing SiC substrates in combination with our sputtering recipe yields films that have higher absorption while maintaining similar transport properties. Thus, geometrically identical detectors can be expected to have a higher detection efficiency with similar electrical performance on SiC compared to SiO_2 substrates. At the same time this can be used to reduce the optical active area of a detector to enhance its electrical properties (for example reducing the fall time) while keeping the same detection efficiency. It is worthwhile to note that the absolute values we obtained for the fall time of SNSPDs are higher than typically measured fall times that are in the order of 10 ns for 10 μm × 10 μm SNSPDs on SiO_2 substrates (measured, e.g. in [74] as well as in our labs). We speculate that the fabrication process of detectors modifies the transport properties of the film such that the kinetic inductivity and thus the fall time are increased compared to the film-derived ones.

3.2. Model of an integrated SNSPD with a triangular cross-section SiC waveguide

In this section, we look into the absorption efficiency of NbTiN based SNSPDs integrated on top of a triangular cross-section SiC waveguides based on the experimental measurements presented in section 3.1. This provides an upper limit for the achievable system detection efficiency of such an integrated detector. The absorption of color center emission (TE- or TM-like) for different configurations of NbTiN was

[4] These are the nominal thicknesses set during the sputtering process and are used in conjunction with the measured deposition rate to calculate the necessary sputtering time. For 6 nm and 10 nm, the thicknesses have also been fitted within the optical model for the ellipsometry data and yielded 5.48(20) nm and 9.62(26) nm.

Table 1. Estimated SNSPD performance metrics from measured film properties. Estimated SNSPD performance metrics from measured film properties. For the derived numbers of the meander SNSPDs we consider 10 μm $\times$ 10 μm detectors with 100 nm wide wires and a fill factor of 50%, while for the double loop SNSPD we assume a 100 nm wide and 40 μm long nanowire, similar to the maximum wire length used in the simulations presented in figures 7 and 8.

				Meander SNSPD		Double loop SNSPD	
Substrate	d (nm)	$I_{dep}(0K)$ (μA)	$I_{dep}(4K)$ (μA)	L_k (μH)	τ_{fall} (ns)	L_k (μH)	τ_{fall} (ns)
SiC	6	14.1	8.9	3.2	63.5	0.254	5.08
	8	38.1	28.7	1.1	22.0	0.088	1.76
	10	75.5	60.3	0.6	11.8	0.047	0.95
SiO_2	8	40.0	30.4	1.0	20.8	0.083	1.66

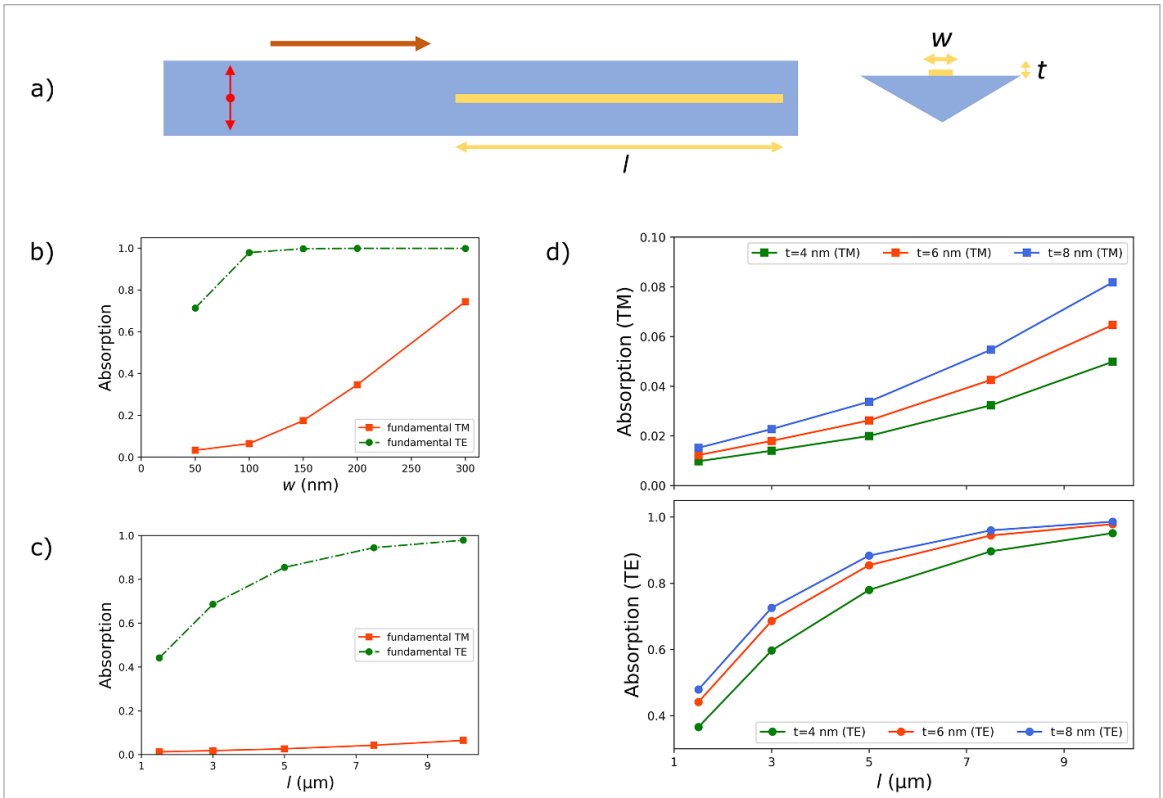

Figure 7. Simulated absorption of a single strip NbTiN layer. (a) Top and cross-section view of a single strip NbTiN (yellow) with length l, width w and thickness t, integrated on a triangular cross-section SiC waveguide (blue). Red dot indicates the color center and red arrows denotes its dipole orientation. Absorption of the f-TE and f-TM modes of the triangular waveguide as a function of (b) width ($l = 10$ μm, $t = 6$ nm). (c) length ($w = 100$ nm, $t = 6$ nm). (d) thickness ($w = 100$ nm).

modeled using the FDTD package in Lumerical software. The NbTiN was modeled using a complex permittivity model with (n, k) values obtained from the ellipsometry measurements discussed in the section 3.1. The top and cross-section view of a single strip of NbTiN integrated on top of a triangular cross-section waveguide are shown in figure 7(a). The single strip has length l, width w, and thickness t, positioned at the center of the top surface of the waveguide.

When the width of the NbTiN strip ($l = 10$ μm, $t = 6$ nm) is increased, the absorption of the f-TE mode remains the same for widths greater than 100 nm and the absorption of the f-TM mode increases as the width increases, as shown in figure 7(b). It should be noted that the absorption of the NbTiN strip is sensitive to the polarization of the mode in the waveguide. The evanescent fields of the f-TE mode are concentrated around the center of the top surface (inset of figure 3(a)), and therefore no changes in absorption are observed for larger SNSPD widths. In comparison, the evanescent fields of the f-TM mode are spread across the entire width of the waveguide (inset of figure 3(c)), requiring larger widths of NbTiN for efficient absorption. As the length ($w = 100$ nm, $t = 6$ nm) and thickness ($w = 100$ nm) of the NbTiN strip increases, the absorption of both the f-TE and f-TM mode increases, as shown in figures 7(c) and (d). Although larger thicknesses would result in better absorption, the single photon detection efficiency decreases [78], which is critical for applications in QIP.

Typical SNSPD based detectors have nanowires fabricated into a meander shape to increase the optical detection area. To this end, we modeled single loop and double loop configurations of NbTiN integrated on

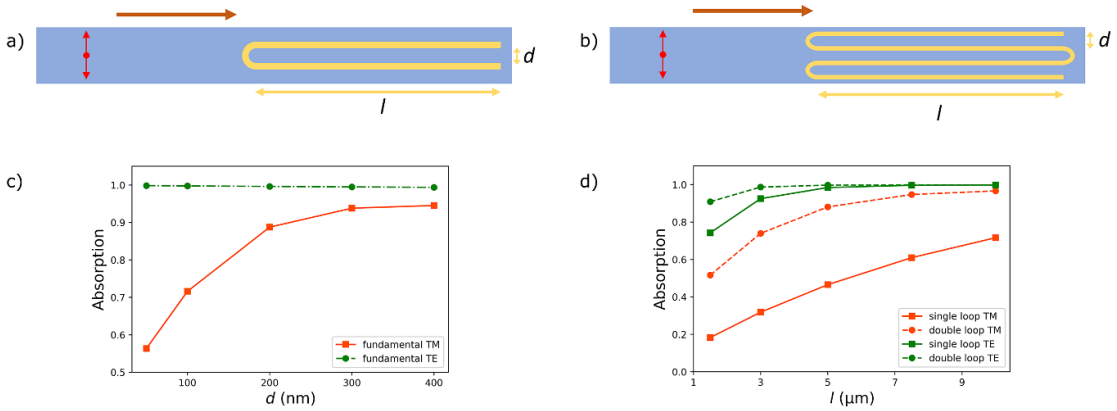

Figure 8. (a) Top-view of a single loop NbTiN (yellow) with length l, spacing between adjacent arms d, on a triangular cross-section SiC waveguide (blue). (b) Top-view of a double loop NbTiN (yellow) with length L, spacing between two adjacent arms d, on a triangular cross-section SiC waveguide (blue). Red dot indicates the color center and red arrows denotes its dipole orientation. (c) Absorption of the f-TE and f-TM modes of the triangular waveguide as a function of spacing between adjacent arms, d ($l = 10$ μm, $w = 10$ nm, $t = 6$ nm). (d) Comparison of absorption of f-TE and f-TM modes of the triangular waveguide as a function of length, for single loop and double loop NbTiN ($w = 100$ nm, $d = 100$ nm, $t = 6$ nm).

top of a triangular cross-section SiC waveguides, as shown in figures 8(a) and (b), respectively. For a single loop NbTiN ($l = 10$ μm, $w = 10$ nm, $t = 6$ nm), as the spacing between two adjacent arms d increases, the absorption of the f-TE mode remains constant and the absorption of the f-TM mode increases rapidly, as shown in figure 8(c). The absorption of the double loop NbTiN ($w = 100$ nm, $d = 100$ nm, $t = 6$ nm) is higher than the single loop NbTiN, with a significant improvement in the absorption of the f-TM mode, as shown in figure 8(d). The polarization sensitivity of the double loop SNSPD at $l = 10$ μm almost disappears, thus having identical detection efficiencies for both f-TE and f-TM modes.

4. Discussion

The results presented in this paper demonstrate scalable approaches to efficiently collect and detect color center emission in triangular cross-section SiC devices for applications in QIP. Triangular cross-section devices are promising for chip scale integration of color center photonics. Moreover, these devices have a rich parameter space (etch angle, width) for optimal color center integration. At a given emission wavelength, there exists an optimal width for each triangular cross-section (with an etch angle alpha) such that the waveguide supports single mode propagation [10], which is important for applications in QIP. The polarization of the color center emission depends on the dipole orientation of the color center with respect to the c-axis. Using 4H-SiC grown along a-plane, most of the color center emission (silicon vacancy, divacancy, nitrogen vacancy) can be coupled into the f-TE mode.

Furthermore, the coupling of the color center emission can be improved by positioning the color center at the maximum intensity point of the f-TE mode, which is around the centroid of the triangular cross-section. Color centers are generated in SiC through implantation of high energy projectiles like electrons, protons, neutrons, ions. The implantation energy and the mass of the implanted particle determine the implantation damage done to the crystal, which can only be partially recovered through annealing [79]. Triangular cross-section devices can be designed depending on the implantation energies available, while still maintaining the single mode propagation and emitter's position at the centroid of the triangular cross-section. The waveguide simulated in this work ($w = 800$ nm, $\alpha = 60°$) has single mode propagation, with ∼44% of the 50% dipole emission (1230 nm) along one direction of the waveguide coupled to the f-TE mode.

The collection efficiency (∼44%) on one end of the designed waveguide can be further improved using a PCM. The periodic variation of the dielectric constant (air holes) in a PC results in a photonic band gap for both TE- and TM-like modes in the waveguide. In a parallel work, a thorough photonic bandgap analysis using PWE method shows that the PCs can be used for a variety of applications and that their dimensions can be scaled depending on the color center emission wavelength [23]. In triangular cross-section PCMs, the TE bandgap is an order of magnitude larger than the TM bandgap, consequently a relatively much smaller complete bandgap. Therefore, a more effective approach for using the PCs as reflectors of c-axis oriented color center emission is to fabricate them in a-plane SiC substrates [10]. This would ensure that a large portion of any color center emission is coupled to the f-TE mode, reflecting frequencies spanning the ZPL

and PSB of the color center emission. FDTD analysis shows that the position of the emitter relative to the PCM determines whether there is constructive/destructive interference in the waveguide region. We highlight that using the PCM proposed in this paper, a randomly positioned emitter has a higher collection efficiency compared to a symmetric waveguide (∼44%) for 75% of cases.

Efficient detection is another important factor for boosting the success rates of QIP protocols. SNSPDs offer a scalable approach for integrating detectors onto photonic devices. On-chip detection using SNSPDs can reduce optical losses, latency, and wiring complexity involved in off-chip detection [28]. As a basis for SiC waveguide integrated SNSPDs, we investigated, for the first time, the optical and electrical properties of NbTiN thin films for SNSPD applications on 4H-SiC substrates. While the absorption of the NbTiN films is significantly higher on SiC than on SiO_2 substrates (up to 50% for photons of 1680 nm), the magneto-electrical properties of the films, and thus presumably also of the detectors, are similar. Provided that the fabrication of SNSPDs on SiC waveguides is of similar quality as on SiO_2 substrates, we expect that they provide comparable electrical performance and simultaneously enhanced system detection efficiency due to higher absorption in the film, making SiC waveguide integrated SNSPDs a promising candidate for on-chip photon detection in QIP.

Data availability statement

The data used for the plots is within the plots and the simulation files used to generate the data is available upon request to the public and is stored on UC Davis servers for 5 years as per the funding agency standards. The data that support the findings of this study are available upon reasonable request from the authors.

Acknowledgment

This work is supported by the National Science Foundation (CAREER-2047564), the Bavaria California Technology Center (BaCaTeC)—Internationalization of the High-Tech-Initiative, the German Federal Ministry of Education and Research via the funding program Quantum technologies—from basic research to market (Contract Numbers 16K1SQ033, 13N15855 and 13N15982) and via the project MARQUAND (Contract Number BN105022) and the Deutsche Forschungsgemeinschaft (DFG, German Research Foundation) under Germany's Excellence Strategy—EXC-2111–390814868.

Conflict of interest

The authors have no conflicts to disclose.

ORCID iDs

Sridhar Majety https://orcid.org/0000-0001-7517-4353
Stefan Strohauer https://orcid.org/0000-0002-3238-5641
Fabian Wietschorke https://orcid.org/0000-0002-3612-211X

References

[1] Norman V A, Majety S, Wang Z, Casey W H, Curro N and Radulaski M 2021 Novel color center platforms enabling fundamental scientific discovery *InfoMat* **3** 869–90
[2] Son N T *et al* 2020 Developing silicon carbide for quantum spintronics *Appl. Phys. Lett.* **116** 190501
[3] Castelletto S, Peruzzo A, Bonato C, Johnson B C, Radulaski M, Ou H, Kaiser F and Wrachtrup J 2022 Silicon carbide photonics bridging quantum technology *ACS Photonics* **9** 1434–57
[4] Zhang G, Cheng Y, Chou J-P and Gali A 2020 Material platforms for defect qubits and single-photon emitters *Appl. Phys. Rev.* **7** 031308
[5] Etzelmüller Bathen M and Vines L 2021 Manipulating single-photon emission from point defects in diamond and silicon carbide *Adv. Quantum Technol.* **4** 2100003
[6] Lukin D M, Guidry M A and Vučković J 2020 Integrated quantum photonics with silicon carbide: challenges and prospects *PRX Quantum* **1** 020102
[7] Majety S, Saha P, Norman V A and Radulaski M 2022 Quantum information processing with integrated silicon carbide photonics *J. Appl. Phys.* **131** 130901
[8] Radulaski M *et al* 2017 Scalable quantum photonics with single color centers in silicon carbide *Nano Lett.* **17** 1782–6
[9] Parker R A *et al* 2021 Infrared erbium photoluminescence enhancement in silicon carbide nano-pillars *J. Appl. Phys.* **130** 145101
[10] Babin C *et al* 2022 Fabrication and nanophotonic waveguide integration of silicon carbide colour centres with preserved spin-optical coherence *Nat. Mater.* **21** 67–73
[11] Lukin D M *et al* 2020 4H-silicon-carbide-on-insulator for integrated quantum and nonlinear photonics *Nat. Photon.* **14** 330–4
[12] Crook A L *et al* 2020 Purcell enhancement of a single silicon carbide color center with coherent spin control *Nano Lett.* **20** 3427–34
[13] Bracher D O, Zhang X and Hu E L 2017 Selective purcell enhancement of two closely linked zero-phonon transitions of a silicon carbide color center *Proc. Natl Acad. Sci.* **114** 4060–5

[14] Calusine G, Politi A and Awschalom D D 2014 Silicon carbide photonic crystal cavities with integrated color centers *Appl. Phys. Lett.* **105** 011123
[15] Calusine G, Politi A and Awschalom D D 2016 Cavity-enhanced measurements of defect spins in silicon carbide *Phys. Rev. Appl.* **6** 014019
[16] Martini F, Gaggero A, Mattioli F and Leoni R 2019 Single photon detection with superconducting nanowires on crystalline silicon carbide *Opt. Express* **27** 29669–75
[17] Martini F, Gaggero A, Mattioli F and Leoni R 2020 Electro-optical characterization of superconducting nanowire single-photon detectors fabricated on 3C silicon carbide *J. Low Temp. Phys.* **199** 563–8
[18] Ferro G 2015 3C-SiC heteroepitaxial growth on silicon: the quest for holy grail *Crit. Rev. Solid State Mater. Sci.* **40** 56–76
[19] Burek M J, De Leon N P, Shields B J, Hausmann B J M, Chu Y, Quan Q, Zibrov A S, Park H, Lukin M D and Lončar M 2012 Free-standing mechanical and photonic nanostructures in single-crystal diamond *Nano Lett.* **12** 6084–9
[20] Song B-S, Jeon S, Kim H, Kang D D, Asano T and Noda S 2018 High-Q-factor nanobeam photonic crystal cavities in bulk silicon carbide *Appl. Phys. Lett.* **113** 231106
[21] Atikian H A, Latawiec P, Burek M J, Sohn Y-I, Meesala S, Gravel N, Kouki A B and Lončar M 2017 Freestanding nanostructures via reactive ion beam angled etching *APL Photonics* **2** 051301
[22] Majety S, Norman V A, Li L, Bell M, Saha P and Radulaski M 2021 Quantum photonics in triangular-cross-section nanodevices in silicon carbide *J. Phys. Photonics* **3** 034008
[23] Saha P, Majety S and Radulaski M 2023 Utilizing photonic band gap in triangular silicon carbide structures for efficient quantum nanophotonic hardware Sci. Rep. 13 4112
[24] Hadden J P, Maynard C, Beggs D M, Taylor R A and Bennett A J 2022 Design of free-space couplers for suspended triangular nano-beam waveguides (arXiv:2207.06157)
[25] Mu Z *et al* 2020 Coherent manipulation with resonant excitation and single emitter creation of nitrogen vacancy centers in 4H silicon carbide *Nano Lett.* **20** 6142–7
[26] Sato S-ichiro, Narahara T, Abe Y, Hijikata Y, Umeda T and Ohshima T 2019 Formation of nitrogen-vacancy centers in 4H-SiC and their near infrared photoluminescence properties *J. Appl. Phys.* **126** 083105
[27] Wang J-F *et al* 2020 Coherent control of nitrogen-vacancy center spins in silicon carbide at room temperature *Phys. Rev. Lett.* **124** 223601
[28] Najafi F *et al* 2015 On-chip detection of non-classical light by scalable integration of single-photon detectors *Nat. Commun.* **6** 1–8
[29] Reithmaier G, Kaniber M, Flassig F, Lichtmannecker S, Müller K, Andrejew A, Vučković J, Gross R and Finley J J 2015 On-chip generation, routing and detection of resonance fluorescence *Nano Lett.* **15** 5208–13
[30] Schwartz M, Schmidt E, Rengstl U, Hornung F, Hepp S, Portalupi S L, Llin K, Jetter M, Siegel M and Michler P 2018 Fully on-chip single-photon hanbury-brown and twiss experiment on a monolithic semiconductor–superconductor platform *Nano Lett.* **18** 6892–7
[31] Elshaari A W, Zadeh I E, Fognini A, Reimer M E, Dalacu D, Poole P J, Zwiller V and Jöns K D 2017 On-chip single photon filtering and multiplexing in hybrid quantum photonic circuits *Nat. Commun.* **8** 1–8
[32] Kim J-H, Aghaeimeibodi S, Carolan J, Englund D and Waks E 2020 Hybrid integration methods for on-chip quantum photonics *Optica* **7** 291–308
[33] Molesky S, Lin Z, Piggott A Y, Jin W, Vucković J and Rodriguez A W 2018 Inverse design in nanophotonics *Nat. Photon.* **12** 659–70
[34] Dory C *et al* 2019 Inverse-designed diamond photonics *Nat. Commun.* **10** 1–7
[35] Joannopoulos J D, Villeneuve P R and Fan S 1997 Photonic crystals: putting a new twist on light *Nature* **386** 143–9
[36] Johnson S G, Fan S, Villeneuve P R, Joannopoulos J D and Kolodziejski L A 1999 Guided modes in photonic crystal slabs *Phys. Rev.* B **60** 5751
[37] Notomi M, Kuramochi E and Taniyama H 2008 Ultrahigh-Q nanocavity with 1D photonic gap *Opt. Express* **16** 11095–102
[38] Quan Q and Loncar M 2011 Deterministic design of wavelength scale, ultra-high Q photonic crystal nanobeam cavities *Opt. Express* **19** 18529–42
[39] Huang L, He D, Mi X, Ding J, Chen S and Peng X 2018 Photonic crystal elliptical-hole tapered low-index-mode nanobeam cavities for sensing *Appl. Opt.* **57** 9822–7
[40] Burek M J, Chu Y, Liddy M S Z, Patel P, Rochman J, Meesala S, Hong W, Quan Q, Lukin M D and Lončar M 2014 High quality-factor optical nanocavities in bulk single-crystal diamond *Nat. Commun.* **5** 1–7
[41] Yusof R, Ali N, Kolenderski P, Slowik K and Ahmad Hambali N A M 2019 Comparative studies of rib waveguide material for quantum communication application *IOP Conf. Ser.: Mater. Sci. Eng.* **551** 012018
[42] Westig M, Thierschmann H, Katan A, Finkel M and Klapwijk T M 2020 Analysis of a single-mode waveguide at sub-terahertz frequencies as a communication channel *AIP Adv.* **10** 015008
[43] Wang J-F *et al* 2020 Experimental optical properties of single nitrogen vacancy centers in silicon carbide at room temperature *ACS Photonics* **7** 1611–6
[44] Zhao D, Yang H, Ma Z and Zhou W 2011 Polarization independent broadband reflectors based on cross-stacked gratings *Opt. Express* **19** 9050–5
[45] Wang R, Wang X-H, Gu B and Yang G-Z 2001 Effects of shapes and orientations of scatterers and lattice symmetries on the photonic band gap in two-dimensional photonic crystals *J. Appl. Phys.* **90** 4307–13
[46] Aravantinos-Zafiris N, Sigalas M M, Kafesaki M and Economou E N 2014 Phononic crystals and elastodynamics: some relevant points *AIP Adv.* **4** 124203
[47] Gol'Tsman G, Okunev O, Chulkova G, Lipatov A, Dzardanov A, Smirnov K, Semenov A, Voronov B, Williams C and Sobolewski R 2001 Fabrication and properties of an ultrafast NbN hot-electron single-photon detector *IEEE Trans. Appl. Supercond.* **11** 574–7
[48] Korzh B *et al* 2020 Demonstration of sub-3 ps temporal resolution with a superconducting nanowire single-photon detector *Nat. Photon.* **14** 250–5
[49] Shibata H, Shimizu K, Takesue H and Tokura Y 2015 Ultimate low system dark-count rate for superconducting nanowire single-photon detector *Opt. Lett.* **40** 3428
[50] Reddy D V, Nerem R R, Nam S W, Mirin R P and Verma V B 2020 Superconducting nanowire single-photon detectors with 98% system detection efficiency at 1550 nm *Optica* **7** 1649
[51] Esmaeil Zadeh I, Chang J, Los J W N, Gyger S, Elshaari A W, Steinhauer S, Dorenbos S N and Zwiller V 2021 Superconducting nanowire single-photon detectors: a perspective on evolution, state-of-the-art, future developments and applications *Appl. Phys. Lett.* **118** 0–14
[52] You L 2020 Superconducting nanowire single-photon detectors for quantum information *Nanophotonics* **9** 2673–92

[53] Polakovic T, Armstrong W, Karapetrov G, Meziani Z E and Novosad V 2020 Unconventional applications of superconducting nanowire single photon detectors *Nanomaterials* **10** 1–20
[54] Marsili F *et al* 2013 Detecting single infrared photons with 93% system efficiency *Nat. Photon.* **7** 210–4
[55] Redaelli L, Bulgarini G, Dobrovolskiy S, Dorenbos S N, Zwiller V, Monroy E and Gérard J M 2016 Design of broadband high-efficiency superconducting-nanowire single photon detectors *Supercond. Sci. Technol.* **29** 1–10
[56] Reithmaier G, Lichtmannecker S, Reichert T, Hasch P, Müller K, Bichler M, Gross R and Finley J J 2013 On-chip time resolved detection of quantum dot emission using integrated superconducting single photon detectors *Sci. Rep.* **3** 1–6
[57] Ferrari S , Schuck C and Pernice W 2018 Waveguide-integrated superconducting nanowire single-photon detectors *Nanophotonics* **7** 1725–58
[58] Makise K, Terai H, Takeda M, Uzawa Y and Wang Z 2011 Characterization of NbTiN thin films deposited on various substrates *IEEE Trans. Appl. Supercond.* **21** 139–42
[59] Banerjee A, Heath R M, Morozov D, Hemakumara D, Nasti U, Thayne I and Hadfield R H 2018 Optical properties of refractory metal based thin films *Opt. Mater. Express* **8** 2072
[60] Hilfiker J N, Singh N, Tiwald T, Convey D, Smith S M, Baker J H and Tompkins H G 2008 Survey of methods to characterize thin absorbing films with Spectroscopic Ellipsometry *Thin Solid Films* **516** 7979–89
[61] Hilfiker J N, Synowicki R a and Tompkins H G 2008 Spectroscopic ellipsometry methods for thin absorbing coatings *51st Annual Technical Conf. Proc. Society of Vacuum Coaters* pp 511–6
[62] Wagner T 2022 private communication
[63] Holzman I and Ivry Y 2019 Superconducting Nanowires for Single-Photon Detection: progress, Challenges and Opportunities *Adv. Quantum Technol.* **2** 1800058
[64] Tanner M G, San Emeterio Alvarez L, Jiang W, Warburton R J, Barber Z H and Hadfield R H 2012 A superconducting nanowire single photon detector on lithium niobate *Nanotechnology* **23** 505201
[65] Bartolf H 2016 *Fluctuation Mechanisms in Superconductors* (Wiesbaden: Springer)
[66] Catelani G and Pekola J P 2022 Using materials for quasiparticle engineering *Mater. Quantum Technol.* **2** 013001
[67] Hazra D *et al* 2018 Superconducting properties of NbTiN thin films deposited by high-temperature chemical vapor deposition *Phys. Rev.* B **97** 1–5
[68] Korneeva Y P, Yu Vodolazov D, Semenov A V, Florya I N, Simonov N, Baeva E, Korneev A A, Goltsman G N and Klapwijk T M 2018 Optical single-photon detection in micrometer-scale NbN bridges *Phys. Rev. Appl.* **9** 64037
[69] Clem J R and Kogan V G 2012 Kinetic impedance and depairing in thin and narrow superconducting films *Phys. Rev.* B **86** 1–16
[70] Bardeen J 1962 Critical fields and currents in superconductors *Rev. Mod. Phys.* **34** 667–81
[71] Khan F V, Khudchenko A, Chekushkin A and Koshelets V P 2022 Characterization of the parameters of superconducting NbN and NbTiN films using parallel plate resonator *IEEE Trans. Appl. Supercond.* **8223** 1–1
[72] Lap B N R, Khudchenko A, Hesper R, Rudakov K I, Dmitriev P, Khan F, Koshelets V P and Baryshev A M 2021 Characterization of superconducting NbTiN films using a dispersive Fourier transform spectrometer *Appl. Phys. Lett.* **119** 152601
[73] Schmidt V V 1997 *The Physics of Superconductors* (Berlin: Springer)
[74] Kerman A J, Dauler E A, Keicher W E, Yang J K W, Berggren K K, Gol'tsman G and Voronov B 2006 Kinetic-inductance-limited reset time of superconducting nanowire photon counters *Appl. Phys. Lett.* **88** 2–5
[75] Smirnov K V, Divochiy A V, Vakhtomin Y B, Sidorova M V, Karpova U V, Morozov P V, Seleznev V A, Zotova A N and Yu Vodolazov D 2016 Rise time of voltage pulses in NbN superconducting single photon detectors *Appl. Phys. Lett.* **109** 052601
[76] Sidorova M, Semenov A D, Hübers H W, Gyger S, Steinhauer S, Zhang X and Schilling A 2021 Magnetoconductance and photoresponse properties of disordered NbTiN films *Phys. Rev.* B **104** 1–10
[77] Steinhauer S, Yang L, Gyger S, Lettner T, Errando-Herranz C, Jöns K D, Amin Baghban M, Gallo K, Zichi J and Zwiller V 2020 NbTiN thin films for superconducting photon detectors on photonic and two-dimensional materials *Appl. Phys. Lett.* **116** 171101
[78] Hofherr M, Rall D, Ilin K, Siegel M, Semenov A, Hübers H W and Gippius N A 2010 Intrinsic detection efficiency of superconducting nanowire single-photon detectors with different thicknesses *J. Appl. Phys.* **108** 014507
[79] Gurfinkel M, Potbhare S, Xiong H D, Suehle J S, Shapira Y, Lelis A J, Habersat D and Goldsman N 2009 Ion implantation and sic transistor performance *J. Appl. Phys.* **105** 084511